

The ALPINE-ALMA [C II] Survey: Star formation-driven outflows and circumgalactic enrichment in the early Universe

M. Ginolfi¹, G. C. Jones^{2,3}, M. Béthermin⁴, Y. Fudamoto¹, F. Loiacono^{5,6}, S. Fujimoto^{7,8}, O. Le Fèvre⁴,
 A. Faisst⁹, D. Schaerer¹, P. Cassata¹⁰, J. D. Silverman^{8,11}, Lin Yan¹², P. Capak⁹, S. Bardelli⁵, M. Boquien¹³,
 R. Carraro¹⁴, M. Dessauges-Zavadsky¹, M. Giavalisco¹⁵, C. Gruppioni⁵, E. Ibar¹⁴, Y. Khusanova⁴,
 B. C. Lemaux¹⁶, R. Maiolino^{2,3}, D. Narayanan¹⁷, P. Oesch¹, F. Pozzi⁶, G. Rodighiero¹⁰, M. Talia^{5,6},
 S. Toft^{18,19}, L. Vallini²⁰, D. Vergani⁵, and G. Zamorani⁵

(Affiliations can be found after the references)

Received XXX; accepted YYY

ABSTRACT

In this work we study the efficiency of galactic feedback in the early Universe by stacking the [C II] 158 μm emission in a large sample of normal star-forming galaxies at $4 < z < 6$, drawn from the *ALMA Large Program to INvestigate [C II] at Early times* (ALPINE) survey. Searching for typical signatures of outflows in the high-velocity tails of the stacked [C II] profile, we observe (i) deviations from a single-component Gaussian model in the combined residuals and (ii) broad emission in the stacked [C II] spectrum, at velocities of $|v| \lesssim 500 \text{ km s}^{-1}$. Interestingly, the significance of these features increases when stacking the sub-group of galaxies with star formation rates (SFRs) higher than the median ($\text{SFR}_{\text{med}} = 25 \text{ M}_{\odot} \text{ yr}^{-1}$), confirming their star formation-driven nature. The estimated typical mass outflow rates are comparable with the SFRs, yielding mass-loading factors of the order of unity (similarly to local normal star-forming galaxies), thus suggesting that star formation-driven feedback does not play a dominant role in quenching galaxies at $z > 4$. From the stacking analysis of the datacubes, we find that the combined [C II] core emission ($|v| < 200 \text{ km s}^{-1}$) of the higher SFR galaxies extends on physical sizes of $\sim 30 \text{ kpc}$ (diameter scale), well beyond the analogous [C II] core emission of lower SFR galaxies and the stacked FIR-continuum. The detection of such extended metal-enriched gas, likely tracing circumgalactic gas enriched by past outflows, corroborates previous similar studies, confirming that baryon cycle and gas exchanges with the circumgalactic medium are at work in normal star-forming galaxies already at early epochs.

Key words. galaxies: evolution - galaxies: formation - galaxies: high-redshift - galaxies: ISM - ISM: jets and outflows - galaxies: star formation

1. Introduction

Current models of galaxy formation widely agree on the key importance of stellar feedback in regulating the evolution of galaxies across the cosmic time. Massive stars ($\gtrsim 8 \text{ M}_{\odot}$) emit copious high-energy photons during their lifetimes and inject energy and momentum in the surrounding gas through Supernovae (SN) explosions, in the final stage of their evolution (see a review by Woosley et al. 2002). These mechanisms can heat the gas and drive turbulent motions in the interstellar medium (ISM; e.g., Dekel & Silk 1986; Mac Low & Ferrara 1999; Hopkins et al. 2012, 2014), reducing the star formation efficiency to the observed typical low values of a few per cent of the free-fall time (e.g., Kennicutt 1998; Krumholz & McKee 2005; Leroy et al. 2008, 2013; Bigiel et al. 2011). Stellar feedback is also often invoked to explain the observed discrepancy between the measured galaxy luminosity (or stellar mass, M_{\star}) function (LF) and the dark matter (DM) halo mass function predicted by the standard cosmological model (e.g., Benson et al. 2003; Silk & Mamon 2012; Behroozi et al. 2013). While the sharp exponential cut-off at the luminous end of the LF is usually ascribed to feedback from accreting black holes (BHs) in active galactic nuclei (AGN; see e.g., Bower et al. 2006; Cattaneo et al. 2009; Fabian 2012), SN-feedback is thought

to be the dominant mechanism in shaping the flat slope at the low-mass end of the LF (e.g., Dekel & Silk 1986; Heckman et al. 1990; Hopkins et al. 2014). In particular, intense episodes of star formation induce powerful SN-driven winds, which can efficiently accelerate the gas to hundreds of km s^{-1} (see e.g., Heckman & Thompson 2017) and eventually expel it from the disk, (i) suppressing the star formation rate (SFR; e.g., Somerville & Davé 2015; Hopkins et al. 2016; Hayward & Hopkins 2017), and (ii) enriching the circumgalactic/intergalactic (CGM/IGM) medium with heavy elements (e.g., Oppenheimer & Davé 2006; Oppenheimer et al. 2010; Pallottini et al. 2014).

Observational evidence of stellar feedback has increased through the years (see Veilleux et al. 2005; Erb 2015 for thorough reviews). A widely adopted method to trace the kinematics of cold and warm outflowing gas consists in measuring the blueshift of metal absorption resonant lines in the rest-frame ultraviolet (UV) and optical bands, with respect to the systemic redshift (usually measured through strong optical emission lines). This technique has been extensively employed to characterise star formation-driven outflows in both local (e.g., Arribas et al. 2014; Chisholm et al. 2015, 2016, 2017; Cicone et al. 2016) and distant galaxies, up to $z \lesssim 3 - 4$ (e.g., Shapley et al. 2003; Steidel et al. 2004,

2010; Rubin et al. 2010; Talia et al. 2012; Rubin et al. 2014; Heckman et al. 2015; Talia et al. 2017).

At higher redshifts, approaching the Epoch of Reionization, detecting outflows through absorption line spectroscopy becomes challenging, mainly because of (i) increasingly weaker metal absorption features, and (ii) large uncertainties on the systemic redshifts, which cannot be obtained from Ly α , whose line-profile is strongly affected by intergalactic absorption and radiative transfer effects. A possible way to overcome such limitations comes from the growing number of recent Atacama Large Millimeter/submillimeter Array (ALMA) observations of bright far-infrared (FIR) lines, e.g., [C II] 158 μm (hereafter [C II]) and [O III] 88 μm at $z > 4$ (see e.g., Wagg et al. 2012; Capak et al. 2015; Maiolino et al. 2015; Inoue et al. 2016; Bradać et al. 2017; Hashimoto et al. 2018; Carniani et al. 2018; Matthee et al. 2019). For instance, combining the redshift determined from [C II] with deep observed-frame optical spectra taken at DEIMOS/Keck, Sugahara et al. (2019) constructed a high-signal to noise (S/N) composite far-UV spectrum of seven Lyman Break Galaxies (LBGs) at $z = 5 - 6$ (Riechers et al. 2014; Capak et al. 2015). They find central outflow velocities (i.e., values measured at the line center, corresponding to the bulk motion of the gas) of $v_{\text{out}} \gtrsim 400 \text{ km s}^{-1}$ and maximum outflow velocities of about 800 km s^{-1} , highlighting an increase (by a factor > 3) with respect to analogue quantities in galaxies at lower redshifts (see Sugahara et al. 2017).

To probe star formation-driven outflows in the early Universe, an alternative method to rest-frame FUV absorption line spectroscopy consists in studying the broad wings in the high-velocity tails of FIR-line spectra, similarly to what is commonly done for luminous AGN-driven outflows (see e.g., Maiolino et al. 2012; Feruglio et al. 2018; Decarli et al. 2018; Bischetti et al. 2019; Stanley et al. 2019). Unfortunately, even significant investments of ALMA time ($\lesssim 1$ hour; see e.g., Capak et al. 2015) do not provide sufficiently good spectra to analyse in details the weak broad components of FIR-lines in individual *normal*¹ star-forming galaxies at $z > 4$, and stacking of large samples would be needed. Some indications of the discovery potential held by FIR-lines stacking analysis come from recent results by Gallerani et al. (2018), who found flux excesses at about $v \pm 500 \text{ km s}^{-1}$ in the stacked residual [C II]-spectrum of a small sample of nine galaxies at $z \sim 5 - 6$ (Capak et al. 2015), likely ascribed to broad wings tracing star formation-driven outflows.

Aiming at improving our understanding of galactic feedback at early epochs, in this paper we explore the efficiency of star formation-driven outflows through the stacking analysis of [C II] emission-lines in a large sample of normal galaxies at $4 < z < 6$, from our *ALMA Large Program to Investigate C* at Early Times* (ALPINE) survey (Le Fèvre et al. 2019; Béthermin et al. 2019; Faisst et al. 2019; see a short description of the survey in Sec. 2). On the one hand, the diversity of ALPINE galaxies (almost 2 dex in SFR and M_{\star} are spanned across the main sequence)

¹ Following the commonly adopted nomenclature in the literature, we use *normal* when referring to galaxies on the *star-forming Main Sequence* (e.g., Brinchmann et al. 2004; Noeske et al. 2007; Daddi et al. 2010; Rodighiero et al. 2011; Speagle et al. 2014).

and the wealth of ancillary multi-wavelength photometric data (from UV to FIR) enable us to investigate primary dependences of stellar outflows on galaxy physical properties. On the other hand, the large statistics provided (the number of [C II]-detected galaxies used for the stacking is ~ 6 -fold higher than similar previous studies; see Gallerani et al. 2018) yields enough sensitivity to (i) map the typical spatial extension of high-velocity outflowing gas and (ii) constrain the circumgalactic enrichment on scales of few tens of kpc, providing new critical pieces of information on the baryon cycling physics that drives the evolution of high- z galaxies.

The paper is organised as follows. In Sec. 2 we describe the ALPINE survey and the data reduction process, while in Sec. 3 we describe the methods of our analysis and report the results. Sec. 4 contains a discussion on the implications of our findings, and Conclusions are summarized in Sec. 5.

Throughout the paper, we assume a flat Universe with $\Omega_{\text{m}} = 0.3$, $\Omega_{\Lambda} = 0.7$ and $H_0 = 70 \text{ km s}^{-1} \text{ Mpc}^{-1}$, and adopt a *Chabrier* initial mass function (IMF; Chabrier 2003).

2. Sample and Observations

ALPINE is an ALMA large program (PI: O. Le Fèvre; Le Fèvre et al. 2019; Béthermin et al. 2019; Faisst et al. 2019) designed to measure [C II] and its surrounding FIR-continuum emission for a representative sample of 118 normal galaxies at $z = [4.4 - 5.8]$. This enables extensive studies of the ISM and dust properties, kinematics and dust-obscured star formation in a representative population of high- z galaxies, with template-fitting derived SFR $\gtrsim 10 M_{\odot} \text{ yr}^{-1}$ and stellar masses in the range $M_{\star} \sim 10^9 - 10^{11} M_{\odot}$. All galaxies have reliable optical spectroscopic redshifts coming from extensive campaigns at the Very Large Telescope (VUDS: Le Fèvre et al. 2015; Tasca et al. 2017) and Keck (Keck-COSMOS: Hasinger et al. 2018, Capak et al. in prep.), and benefit from a wealth of ancillary multi-wavelength photometric data (from UV to FIR; see Faisst et al. in prep.). This makes ALPINE one of the currently largest panchromatic samples to study the physical properties of normal high- z galaxies (see a discussion in Le Fèvre et al. in prep., and Faisst et al. 2019).

The overall ALMA observational strategy/setup and details on the data reduction steps (including data quality assessment) are comprehensively discussed in Béthermin et al. in prep., but a short summary of relevant information is reported here. ALMA observations were carried out in Band-7 during Cycle 5 and Cycle 6, and completed in February 2019. Each target was observed between 20 minutes and 1 hour of exposure time, with phases centred at the rest-frame UV positions of the sources. One spectral window was centred on the [C II] expected frequencies, according to the spectroscopic redshifts extracted from UV-spectra, while other side-bands were used for continuum measurements. The data were calibrated using the Common Astronomy Software Applications package (CASA; McMullin et al. 2007), version 5.4.0, and additional flagging of bad antennas was performed in a few cases (see Béthermin et al. in prep.). Continuum maps were obtained running the CASA task `clean` (multi-frequency synthesis mode) over the line-free visibilities in all spectral

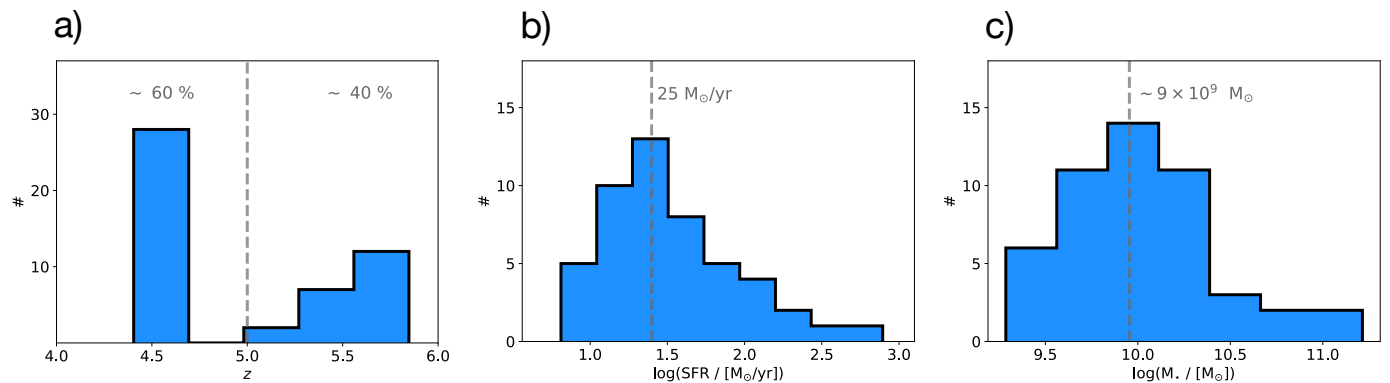


Fig. 1. Redshift (a), SFR (b), and M_* (c) distributions of our final sample of normal galaxies drawn from the ALPINE survey and used in this work (see Sec. 3.1.2). The gap in the redshift distribution is due to the original ALPINE sample selection, tailored to avoid a prominent atmospheric absorption at ~ 325 GHz, in the ALMA band 7. The grey dashed lines in panels b) and c) represent the median SFR and M_{star} of our galaxies.

windows, while [C II] datacubes were generated from the continuum-subtracted visibilities, with 500 iterations and a S/N threshold of $\sigma_{\text{clean}} = 3$ in the `clean` algorithm. We chose a natural weighting of the visibilities, a common pixel size of $0.15''$ and a common spectral bin of 25 km s^{-1} (resulting to be the best compromise in terms of number of spectral elements to resolve the line and S/N per channel). The median sensitivity (in the spectral regions close to [C II] frequencies) reached by the cubes in our sample is $\sim 0.35 \text{ mJy/beam}$ for a 25 km s^{-1} spectral channel, while the overall distribution ranges between 0.2 and 0.55 mJy/beam per channel with the same velocity binning. Such a variation (notwithstanding similar integration times) is mainly driven by the redshift range covered by our targets and the evolving atmospheric transmissivity function in ALMA Band-7 (see Béthermin et al. in prep.). The typical angular resolution of the final products, computed as the average circularized beam axis, is $0.9''$ ($\sim 5.2 - 6 \text{ kpc}$ in the redshift range $z = 4.4 - 5.8$), with values ranging between $0.8'' - 1''$. In Béthermin et al. in prep., we discuss in details the methods adopted to extract continuum and [C II] information from ALPINE observations, while we refer to other forthcoming works for an overview of ALPINE-related results. The data-set consists of 75 robustly [C II]-detected galaxies², with a S/N > 3.5 (i.e., the threshold at which our simulations indicate a 95% reliability; see Béthermin et al. in prep.) calculated as the ratio between peak fluxes and rms in optimally-extracted³ [C II] velocity-integrated maps.

3. Analysis and Results

[C II] is the brightest line in the FIR spectra of star-forming galaxies and it has been exploited to trace AGN-driven outflows revealed by the presence of broad wings in the spectra of luminous high- z QSOs (see e.g., Maiolino et al. 2012; Ciccone et al. 2015; Janssen et al. 2016; Feruglio et al. 2018; Decarli et al. 2018; Bischetti et al. 2019; Stanley et al.

² Note that, as discussed in Sec. 3, in this work we exclude from our analysis $\sim 30\%$ of the sample, consisting of merging systems.

³ Velocity-Integrated [C II] maps were created in an iterative way, allowing for (i) slight (astrometry-corrected) spatial offsets ($< 1''$) between the [C II] and rest-frame UV centroids, and (ii) spectral shifts between [C II] line and expected frequencies from UV-spectra (see Béthermin et al. in prep., for details).

2019). In normal galaxies, where outflows are expected to be more powered by stellar feedback rather than AGN-activity, broad wings are expected to be less prominent and weaker (see, e.g., a review by Heckman & Thompson 2017); therefore, even in the deepest currently available [C II] observations at $z \gtrsim 4$, the sensitivity is generally not adequate to detect weak broad components in individual objects (e.g., Capak et al. 2015; Maiolino et al. 2015; Gallerani et al. 2018; Fujimoto et al. 2019).

In order to explore the efficiency of galactic feedback at play in normal star-forming galaxies in the early Universe, we perform a stacking analysis of the [C II] emission in a sample of galaxies (see Sec. 3.1.2) drawn from the ALPINE survey (see Sec. 2). The stacking technique enables us to substantially increase the sensitivity in the combined spectra/cubes. It therefore holds a significant discovery potential as shown in Bischetti et al. (2019) and Gallerani et al. (2018), who successfully carried out the stacking of a QSO sample at $4.5 < z < 7$, and a small sample of normal galaxies at $z \sim 5$, respectively. In the following we describe the methods used to extract, align and stack [C II] spectra and cubes of our galaxies, and report the results.

3.1. Methods and Stacking Analysis

Our analysis is based on three different procedures (described in the next paragraphs), each of them providing complementary information:

- stacking of the **residuals**, computed by subtracting a single-component Gaussian fit to each [C II] spectrum (Sec. 3.2). This procedure is needed to test whether or not a single-Gaussian component is sufficient to describe (on average) our [C II] spectra;
- stacking of the **[C II] spectra** (Sec. 3.3), to verify the improvement gained in describing the combined spectrum with a two-components Gaussian model, and to compute the typical outflow properties (e.g., velocity and mass of the neutral atomic gas);
- stacking of the **[C II] cubes** (Sec. 3.4), to obtain information on the typical spatial distribution of the [C II] emission, both at low- and high-velocities.

3.1.1. Extraction of spectra and alignment

To extract the [C II] spectra of our galaxies we use 2D-apertures defined by the pixels contained within the 2σ -levels of our optimally-extracted [C II] velocity-integrated maps (see Béthermin et al. in prep.). Rather than adopting a common fixed aperture, this has the advantage of taking into account variable morphologies/extensions of the gas, in order to include most of the flux coming from the total [C II]-emitting region, and to minimise the addition of noise. However, as discussed in Sec. 3.3, we also tested fixed and smaller apertures.

Before stacking, we align the spectral axes of both spectra and cubes according to their [C II] observed frequencies: we set as a common *zero-velocity* reference the 25 km s^{-1} -sized channel/slice centred (after interpolation) on the centroid frequency of the Gaussian fit. The resulting distribution of the number of objects per spectral element (as shown in the top panels of the next figures, e.g., Fig. 2, 3) is not uniform along the full velocity-range and declines starting from a few hundreds of km s^{-1} around the line, up to halving at about $\pm 1000 \text{ km s}^{-1}$. These effects are mainly due to: (i) the exclusion of a few spectral channels flagged by the pipeline during the reduction steps, and more importantly (ii) spectral offsets between the *observed* [C II]-redshifts and the *expected* redshifts as derived from rest-frame UV spectra, originally used to centre the spectral windows (see Béthermin et al. in prep. and Cassata et al., in prep., for technical details and a physical interpretation of the velocity offsets, respectively).

We also spatially align the [C II] cubes, centering them on the brightest pixel of [C II] velocity-integrated maps. This procedure is preferred to choosing the phase centre (coincident with the centroid of rest-frame UV positions of the sources) as a common spatial reference point, since a few sources show small spatial offsets ($< 1''$, whose physical interpretation will be discussed in another paper) between the [C II] and optical images centroids⁴.

3.1.2. Exclusion of possible contaminants

As explained in Sec. 3.1 and discussed in the next paragraphs, in this work we are interested in revealing deviations from a single-component Gaussian model and flux-excesses in the high-velocity tails of the stacked spectra and cubes possibly due to SF-driven winds. Since these effects may be mimicked by companion galaxies and satellites in interacting systems (see discussions in e.g., Gallerani et al. 2018; Fujimoto et al. 2019; Pallottini et al. 2019), we exclude from our analysis 25 objects (corresponding to $\sim 30\%$ of the [C II]-detected ALPINE sample) with signs of ongoing major/minor mergers; for those systems a proper spatial or spectral deblending cannot be performed and any attempt does not guarantee to remove possible contamination. Such selection is based on a morpho-kinematic classification, described in detail in Le Fèvre et al. in prep., and performed combining information

⁴ For the sake of clarity we repeated our analysis leaving the phase centres as common spatial reference points, and the results of cube-stacking are identical within the errors. The lack of evident deviation is due to the fact that only a small fraction ($< 10\%$) of our sample is affected by small offsets ($< 1''$) between [C II] and rest-frame UV (see a discussion in a similar analysis by Fujimoto et al. 2019).

from the ancillary multi-wavelength photometry and the ALMA products (e.g., velocity-integrated [C II] maps, 2D kinematics maps, and position-velocity diagrams; see Jones et al. in prep.). We note that our exclusion of interacting systems does not prevent the sample from being somehow still contaminated by unresolved, HST/ALMA undetected, faint satellites⁵. While, as discussed in the next sections, some arguments suggest that this effect should not be significant, a more solid solution to this caveat could be only provided in the future by deeper and higher-resolution observations.

The final sample, drawn from ALPINE and used in this work, consists of 50 normal star-forming galaxies at redshift $4.4 < z < 5.8$ (Fig. 1.a), with SFR $\sim 5 - 600 \text{ M}_\odot \text{ yr}^{-1}$ (Fig. 1.b) and $\log(M_\star/M_\odot) \sim 9 - 11$ (Fig. 1.c). Stellar masses and star formation rates are derived from Bruzual & Charlot (2003) composite stellar population template fitting, using the LePhare code (Arnouts et al. 1999; Ilbert et al. 2006) with a large range in stellar ages, metallicities, and dust reddening. For further details we refer the reader to Faisst et al. in prep.

3.2. Combining the residuals

Before searching for signatures of star formation-driven outflows in the high-velocity tails of the stacked [C II] spectrum, we check the *null hypothesis* that the [C II] line profiles of our galaxies are well (and completely) described by a single-Gaussian model. We therefore perform the simple standard procedure (see e.g., Gallerani et al. 2018) described in the following:

- (i) we fit a single-Gaussian profile to each [C II] spectrum (where the peak flux, centre velocity⁶ and full width at half maximum, FWHM, are free parameters), and compute the model value G_i , in each independent 25 km s^{-1} -sized spectral bin i ;
- (ii) for each spectrum we compute the residuals R_i , by subtracting in each channel the best-fitting Gaussian model G_i to the observed flux F_i , i.e., $R_i = F_i - G_i$;
- (iii) we combine the residuals performing a variance-weighted stacking:

$$R_i^{\text{stack}} = \frac{\sum_{k=1}^N R_{i,k} \cdot w_k}{\sum_{k=1}^N w_k}, \quad (1)$$

where N is the number of galaxies contributing to each velocity bin, and the weighting factor w_k is defined as $w_k = 1/\sigma_k^2$, where σ_k is the spectral noise associated with the spectrum k . We compute σ_k as the root mean square (rms) of the noise contained in each spectrum excluding channels in the velocity range $[-800 : +800] \text{ km s}^{-1}$ around the centre, to avoid the [C II] emission line of the galaxies themselves⁷.

⁵ We estimate a limit of $\lesssim 1.5 \text{ M}_\odot \text{ yr}^{-1}$ on their SFR, based on the absolute UV magnitude limit of our sample.

⁶ Note that, since the spectra were spectrally centred and aligned at $z_{[\text{CII}]}$ (as discussed in Sec. 3.1.1), the centre velocity is by definition 0 km s^{-1} .

⁷ We found $\pm 800 \text{ km s}^{-1}$ to be an optimal compromise between (i) having a large number of independent spectral bins to use for the determination of noise and (ii) conservatively excluding the

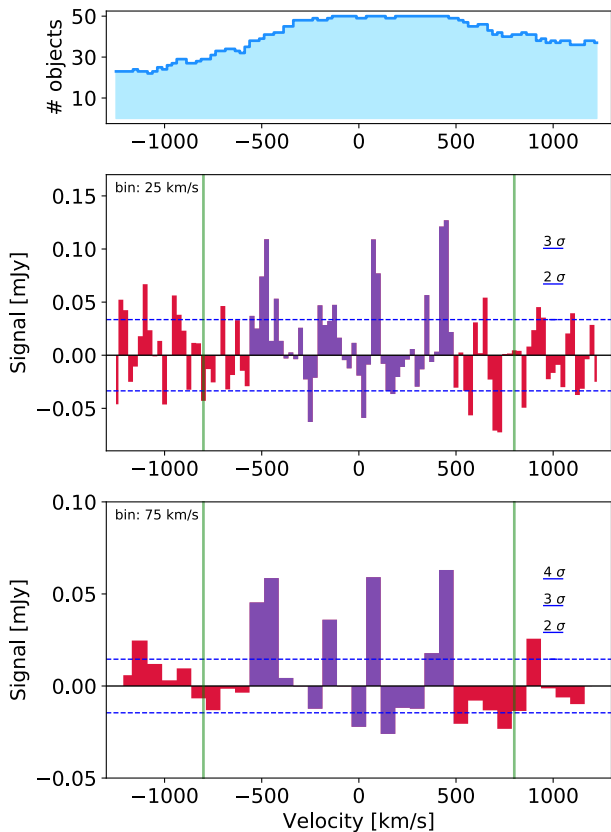


Fig. 2. The top panel shows a histogram containing the number of objects per channel contributing to the stacked flux. In the central (lower) panel the variance-weighted stacked [C II] residuals from a single-Gaussian fit are shown, in spectral bins of 25 km s^{-1} (75 km s^{-1}). The green solid lines at $\pm 800 \text{ km s}^{-1}$ enclose the velocity range excluded for the estimation of spectral noise, while the blue dashed lines represent the spectral rms at $\pm 1\sigma$. Channels in violet represent the channels in the velocity range enclosed by the outermost peaks at $\geq 3\sigma$ in the 75 km s^{-1} -binned stacked residuals. This helps in visualizing the velocity interval affected by flux excesses.

In Fig. 2 we show the resulting stacked residuals, R_i^{stack} , where, for each spectral channel i , we report on the top panel the number of sources contributing to the corresponding flux. In the velocity range $v \sim [-500 : +500] \text{ km s}^{-1}$ we find peaks of flux excess with significance $> 3\sigma$ (where σ is computed as the ratio between R_i^{stack} and σ_k) in single velocity bins (see violet bins, whose definition is reported in the caption of Fig. 2), while the flux distribution in the stacked residuals at larger velocities ($|v| > 600 \text{ km s}^{-1}$) is completely consistent with the noise. To facilitate the interpretation and improve the visualization, we re-bin the stacked residuals in channels of 75 km s^{-1} (averaging over three contiguous spectral elements), revealing an increase of the flux excess significance up to 4σ in the velocity range $v \sim [-500 : +500] \text{ km s}^{-1}$.

We note that in the hypothesis that our [C II] spectra were completely described by a single-Gaussian profile, the resulting flux from the stacked residuals should be simply consistent with random noise over the full velocity range.

velocity range usually found to be affected by stellar outflows. The effectiveness of this choice is probed *a posteriori* by our own results, since (as discussed in the following) no significant residuals are found at $|v| > 600 - 700 \text{ km s}^{-1}$.

To explore the origin of such observed deviations from a single-Gaussian profile and probe any connection with stellar feedback, we repeat the analysis described above dividing our sample in two SFR-defined bins, and analysing each of them individually. Specifically, we use the median SFR of galaxies in our sample ($\text{SFR}_{\text{med}} = 25 \text{ M}_{\odot} \text{ yr}^{-1}$; see Fig. 1.b) as the threshold to create two equally populated sub-samples of *low*-SFR galaxies ($\text{SFR} < 25 \text{ M}_{\odot} \text{ yr}^{-1}$) and *high*-SFR⁸ galaxies ($\text{SFR} > 25 \text{ M}_{\odot} \text{ yr}^{-1}$). We find that:

- the stacked residuals of low-SFR galaxies do not show any clear sign of significant flux-excess over the entire velocity range, as shown in Fig. 3.a. Channels at $v \sim [-500 : +500] \text{ km s}^{-1}$ (where positive signal is detected when stacking the full sample; see Fig. 2) are noise-dominated, with only few (one) channels exceeding 2σ in the 25 km s^{-1} (75 km s^{-1})-binned spectrum;
- flux excess at $|v| \lesssim 500 \text{ km s}^{-1}$ in the stacked residuals of high-SFR galaxies is more distinct than in the stacked residuals of the full sample, with (i) a larger number of connected velocity bins at $\text{S/N} > 3\sigma$, and (ii) peaks reaching an increased significance of 4σ (5σ) in the 25 km s^{-1} (75 km s^{-1})-binned spectrum. At lower velocities, $v \sim [-300 : +300] \text{ km s}^{-1}$, the residuals look flatter, with some weak symmetric negative peaks⁹ at about $v \pm 250 \text{ km s}^{-1}$.

Therefore, the most star-forming galaxies in our sample contribute more to the deviation from a single-Gaussian profile, indicating a possible connection (on average) between the amount of SFR and the observed deviation from a single-component Gaussian profile in the [C II] spectra of high- z normal galaxies. Altogether, these findings suggest that the star formation (or, more properly, star formation-driven mechanisms) is likely to be responsible for producing the observed flux excess at the high-velocity tails of the stacked residuals.

3.2.1. Any contribution from rotating galaxies?

While dispersion-dominated galaxies exhibit single-peak spectra, the double-horned profiles of rotating disks (see e.g., Begeman 1989; Daddi et al. 2010; de Blok et al. 2016; Kohandel et al. 2019) are not well described by a single Gaussian. In addition, evidence for rotating disks has been found at high-redshift (e.g., De Breuck et al. 2014; Jones et al. 2017; Talia et al. 2018; Smit et al. 2018). Thus, it is conceivable that the presence of rotating disks in our sample may contribute to the deviation from a single-Gaussian (see e.g., Kohandel et al. 2019) and to produce the symmetric residuals seen in Fig. 3. However, we note that large rotational velocities of $|v| \sim 500 \text{ km s}^{-1}$ have been observed only

⁸ The labels *low* and *high* are specifically referred to the SFR-distribution of galaxies in our sample.

⁹ The symmetric weak negative peaks at about $v \pm 250 \text{ km s}^{-1}$ are consistent with the negative residuals obtained from a single-Gaussian fit of a curve that is better described by the combination of a narrow and a broad Gaussian components (see Sec. 3.3).

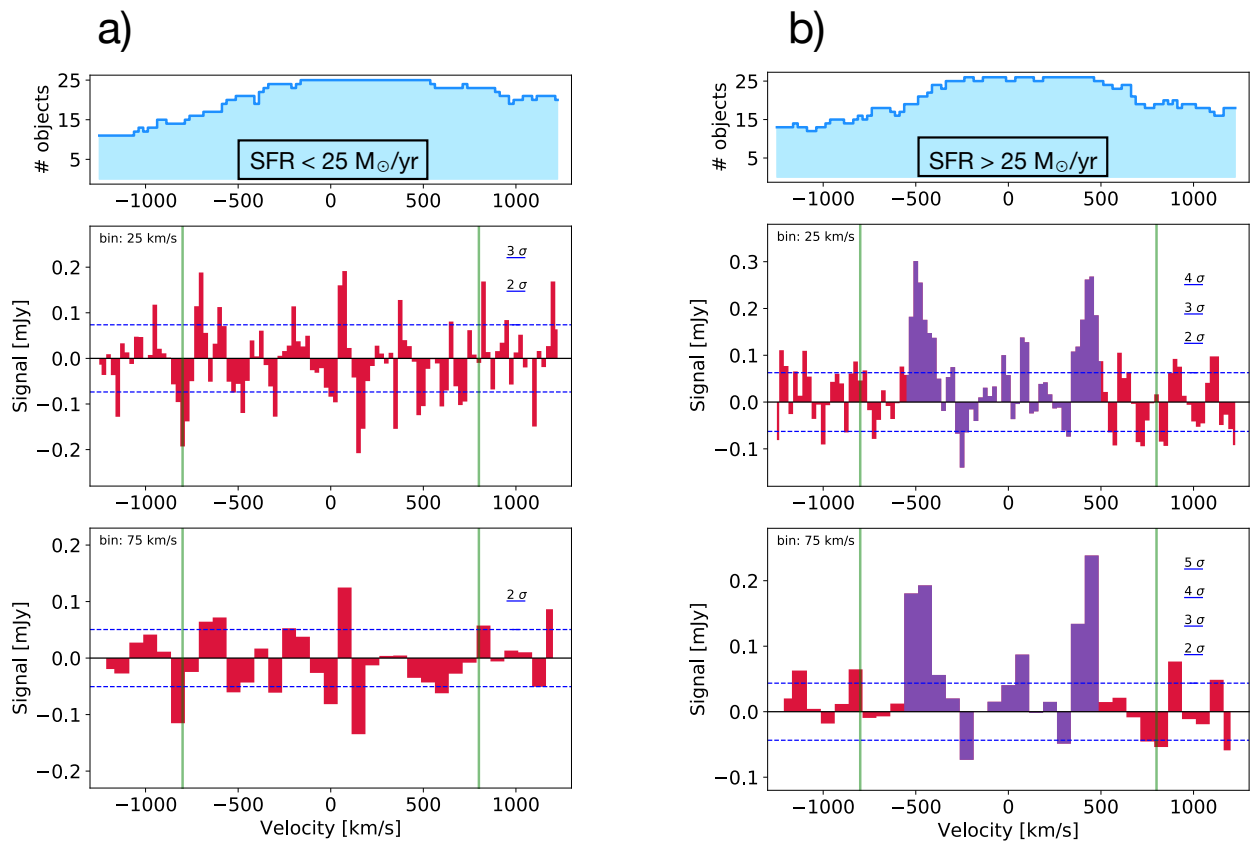


Fig. 3. Same description of Fig. 2. In this case the stacked residuals are shown for the low-SFR (a), and the high-SFR (b) groups, individually. While the stacked residuals are consistent with the noise in the low-SFR sub-sample, significant ($> 4\sigma$) peaks of flux excess are detected for high-SFR galaxies.

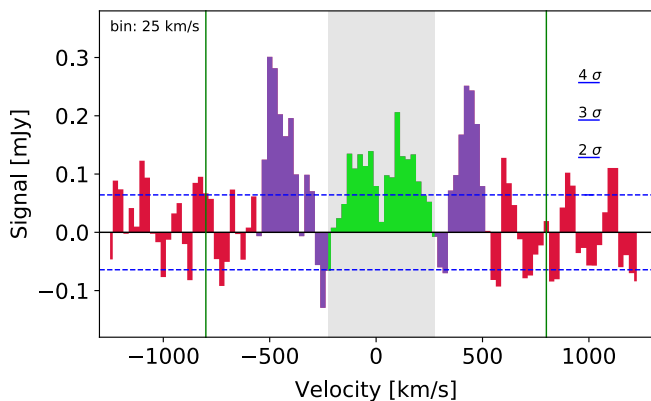


Fig. 4. Similarly to the central panel of Fig. 3.b, the 25 km s^{-1} -binned stacked [C II] residuals of the high-SFR group are shown. However, here, for the five rotators in the sub-sample, $R_{i,k}$ (see Eq. 1) is calculated by subtracting a kinematic model to the observed spectra. We colour in green the channels where the residuals left by the tilted-ring fit are non-null, specifically in the velocity range $v \sim [-225 : +275]$ km s^{-1} , marked by the grey shaded region.

in bright sub-mm galaxies (SMGs) and AGN-host galaxies, with intense SFRs $\geq 1000 M_{\odot} \text{ yr}^{-1}$ and very broad FWHMs ≥ 800 km s^{-1} (see e.g., Carniani et al. 2013; Jones et al. 2017; Talia et al. 2018), and are unlikely to be produced by normal star-forming rotating galaxies (the median FWHM of [C II] profiles in our high-SFR galaxies is ~ 250 km s^{-1}).

In order to further explore this argument we use $3^{\text{D}}\text{BAROLO}$ (a tool for fitting 3D tilted-ring models to emission-line datacubes that takes into account the effect of beam smearing; see Di Teodoro & Fraternali 2015) to build kinematic models of five galaxies classified as rotators (Le Fèvre et al., in prep.) in the high-SFR group, for which we have enough independent spatial elements to obtain robust fits (see details in Jones et al., in prep.). We then repeat the residuals-stack of our high-SFR galaxies, but now, for the five ALPINE rotators modelled with $3^{\text{D}}\text{BAROLO}$, we calculate $R_{i,k}$ (see Eq. 1) by subtracting the tilted-ring fit to the observed spectra, rather than the Gaussian model. The resulting stacked residuals are shown in Fig. 4: while peaks of flux excess resulting from the kinematic modelling are indeed visible in the residuals (see green channels), these are more concentrated toward the common reference centre, only affecting the velocity range $v \sim [-225 : +275]$ km s^{-1} (see grey shaded region). This test suggests that the effect of unresolved kinematics in the spectra of our normal rotating galaxies should not have a significant impact on the residuals observed at $|v| \lesssim 500$ km s^{-1} , whose origin should be ascribed to other mechanisms, as discussed below.

3.3. Stacking the spectra

In Sec. 3.2 we discussed that a single-Gaussian component is not sufficient to correctly model (on average) the [C II] spectra of a representative (see M_{\star} and SFR distributions in Fig. 1) population of high- z normal galaxies (Fig. 2). In particular, we found that the deviation from a single-Gaussian

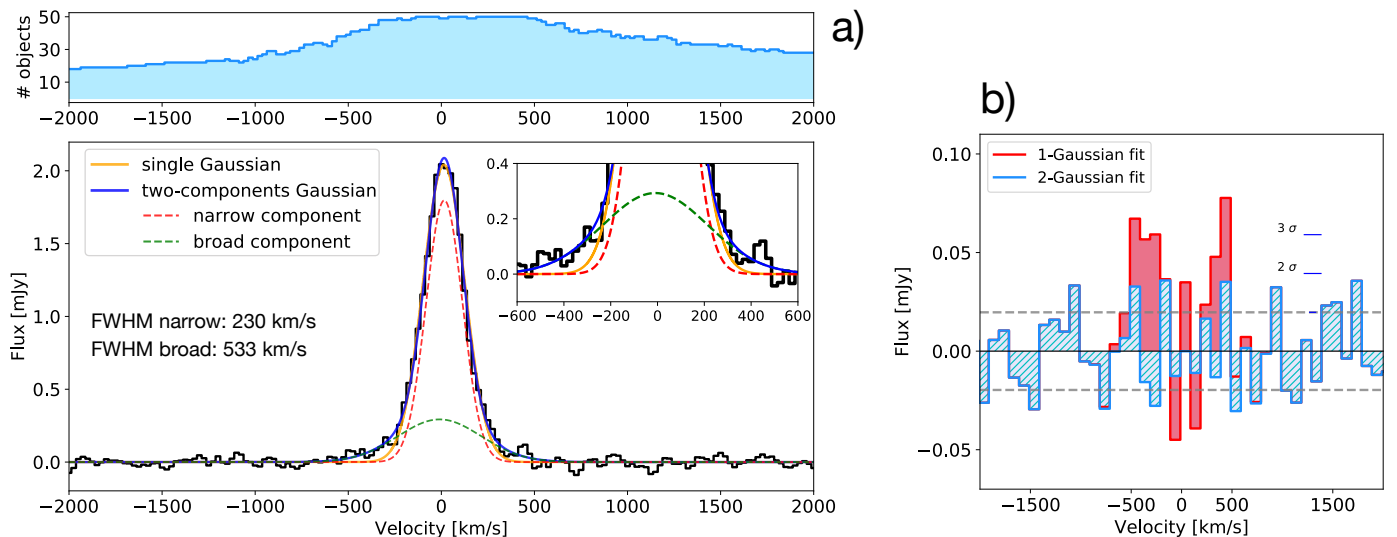


Fig. 5. a) The variance-weighted stacked [C II] spectrum of all galaxies in our sample is shown, in velocity bins of 25 km s^{-1} . The orange (blue) line shows the single-Gaussian (two-Gaussian) best-fit. The red and the green line represent the narrow and broad components of the two-Gaussian model, respectively. A zoom of the velocity range $[-600 : +600] \text{ km s}^{-1}$ is shown in the inset. A histogram containing the number of objects per channel contributing to the stacking is shown in the top panel. b) Residuals from the single-Gaussian (two-Gaussian) best-fit are shown in red (blue), in velocity bins of 50 km s^{-1} .

model is related to the SFR, with high (low)-significance flux excess found in the stacked residuals of high (low)-SFR galaxies (Fig. 3). Interestingly, in line with previous similar works (e.g., Gallerani et al. 2018), most of the positive signal revealed in the stacked residuals of highly star-forming galaxies arises from almost symmetric high-velocity tails (see Fig. 3.b), specifically at velocities consistent with those observed through UV-spectroscopy in the outflowing gas accelerated by stellar feedback at similar redshifts (e.g., Sugahara et al. 2019; see a discussion in Sec. 1). This suggests that the observed flux excess can be ascribed to SFR-driven outflows. However, to corroborate this hypothesis we need to test whether a two-components Gaussian model, i.e., a combination of a narrow plus a broad component (with the latter tracing the outflowing gas; see Sec. 3), can better describe our observations.

We therefore perform a variance-weighted stacking of the [C II] spectra of galaxies in our sample, to compute (and compare) the residuals of single-Gaussian and two-components Gaussian best fits. In analogy with Eq. 1, each i -th channel of the stacked spectrum S_i^{stack} is defined as:

$$S_i^{\text{stack}} = \frac{\sum_{k=1}^N S_{i,k} \cdot w_k}{\sum_{k=1}^N w_k}, \quad (2)$$

where $S_{i,k}$ is the [C II] spectrum of the k -th galaxy, and the weighting factor $w_k = 1/\sigma_k^2$ is calculated as described in Sec. 3.2.

In Fig. 5.a we show the [C II] spectrum resulting from the stacking of our full sample (with a spectral element binning of 25 km s^{-1}) along with the single- and two-components Gaussian best fits. As for the figures in Sec. 3.2, a histogram reporting the number of objects per channel contributing to the corresponding flux is shown on the top panel. The stacked [C II] spectrum appears to be clearly characterised by weak (less than 10% of the line peak-flux) broad wings at velocities of few hundreds of km s^{-1} (see inset in Fig. 5.a). We find that, while a

single-Gaussian fit produces significant positive residuals at $v \sim \pm[300 : 500] \text{ km s}^{-1}$ (in agreement with results from Sec. 3.2), a two-components Gaussian fit can accurately describe the stacked spectrum, leaving residuals that are reasonably consistent with simple noise (no peaks exist at $> 2\sigma$; see Fig. 5.b). Our two-Gaussian model best fit results in a combination of a narrow component and a relatively less prominent broad component, in agreement with typical line profiles observed in presence of outflows at low- z or in AGN-host galaxies (see a discussion in Sec. 1). Both the narrow and broad Gaussian components are centred at the stacked [C II] line-peak ($v_{\text{cen}} \sim 0 \pm 10 \text{ km s}^{-1}$). We measure a $\text{FWHM} = 230 \pm 15 \text{ km s}^{-1}$ for the narrow component, and a $\text{FWHM} = 533 \pm 80 \text{ km s}^{-1}$ for the broad component¹⁰.

In analogy with the analysis carried out on the stacked residuals, we test the dependence of the average [C II] spectral properties on the SFR, dividing our sample in two SFR bins as described in Sec. 3.2, and repeating the analysis in each group. We find that:

- the stacked [C II] spectrum of low-SFR galaxies ($\text{SFR} < 25 M_{\odot} \text{ yr}^{-1}$) does not show clear signs of broad wings (see Fig. 6.a). As expected, given a larger number of free parameters, the residuals left by the two-components Gaussian best fit are lower than in the single-Gaussian case. However, although somehow more pronounced at $v \sim [-500 : +500] \text{ km s}^{-1}$, the residuals produced by the single-Gaussian best fit are generally consistent with the noise (no peaks at $\geq 3\sigma$), indicating that the low-SFR galaxies stacked spectrum can be sufficiently well described by a single-component Gaussian profile. Moreover, in this case the two-components Gaussian best fit is not determined by the expected combination

¹⁰ Here and in the following, the reported FWHM values are deconvolved for the intrinsic spectral resolution of the stacked spectra (25 km s^{-1}), while the associated uncertainties are estimated through a bootstrap analysis, as described in the next paragraphs.

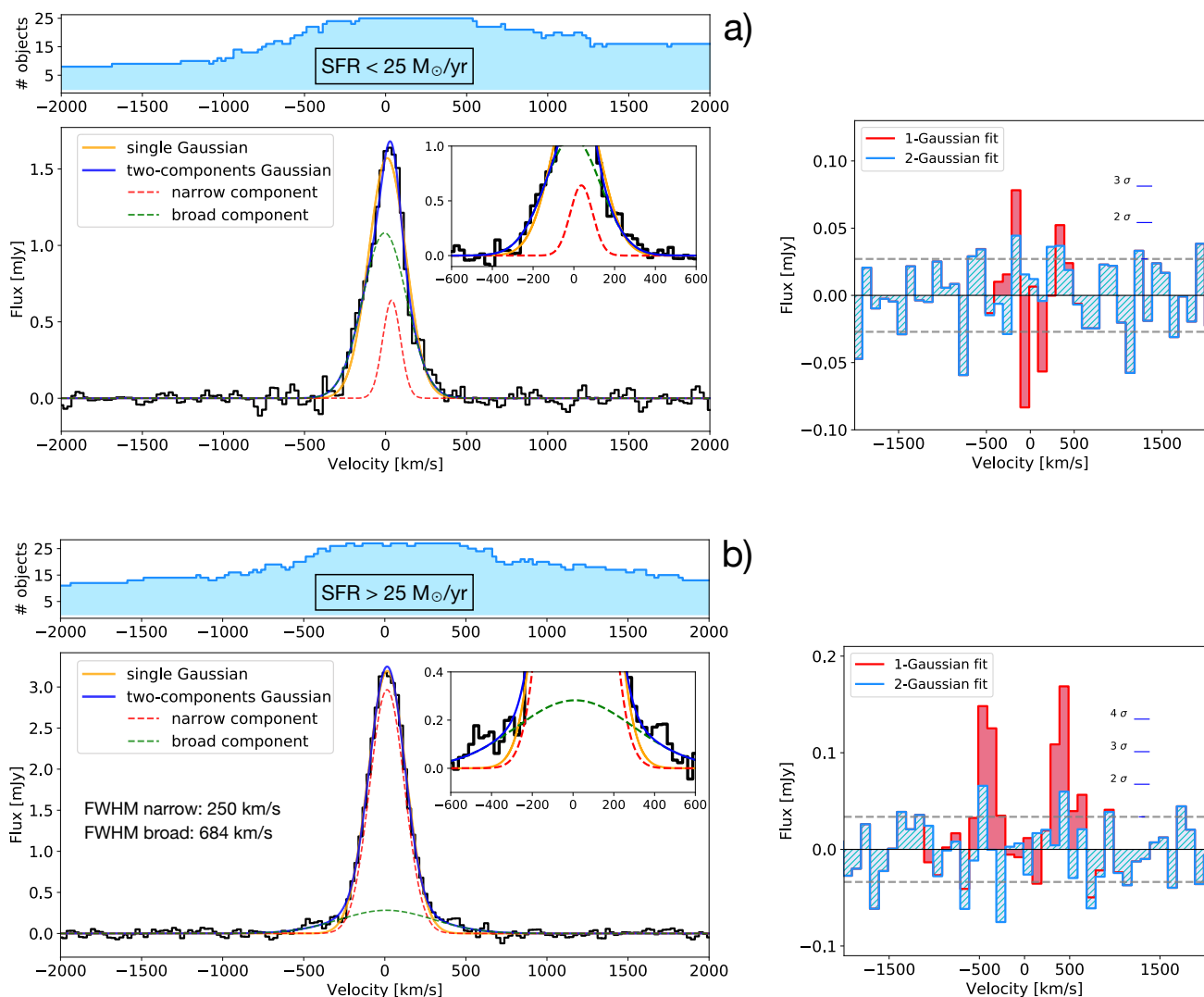


Fig. 6. Same description of Fig. 5. In this case the stacked [C II] spectrum and corresponding residuals from a single- and two-Gaussian best-fits are shown for the low-SFR (a), and the high-SFR (b) sub-samples, individually.

of a narrow and (less prominent) broad component, and therefore does not provide meaningful result;

- the stacked [C II] spectrum of high-SFR galaxies ($\text{SFR} > 25 M_{\odot} \text{ yr}^{-1}$) shows clear signs of broad wings on the high-velocity tails, at $v \pm \sim 500 \text{ km s}^{-1}$ (see Fig. 6.b). The single-Gaussian best fit leaves significant residuals (with peaks exceeding 4σ) in the velocity range $v \sim \pm[300 : 500] \text{ km s}^{-1}$, more prominent than the residuals found in the combined spectrum from the full sample. On the other hand, the two-components Gaussian best fit, resulting in a combination of a narrow ($\text{FWHM} = 250 \pm 10 \text{ km s}^{-1}$) and a broad ($\text{FWHM} = 684 \pm 65 \text{ km s}^{-1}$) component, produces residuals that are fully consistent with the noise.

These findings do not prove the absence of a broad component (i.e., a possible signature of outflows) in the stacked spectrum of the low-SFR sub-sample. Indeed, since [C II] is generally fainter in low-SFR galaxies (see e.g., Capak et al. 2015; Carniani et al. 2018; Matthee et al. 2019; Schaerer et al., in prep.), we might expect this feature to be less evident and most likely below the detection limit.

	Full Sample	High-SFR group
SFR_{med}	$25 M_{\odot} \text{ yr}^{-1}$	$50 M_{\odot} \text{ yr}^{-1}$
FHWM - narrow	$230 \pm 15 \text{ km s}^{-1}$	$250 \pm 10 \text{ km s}^{-1}$
FHWM - broad	$533 \pm 80 \text{ km s}^{-1}$	$684 \pm 65 \text{ km s}^{-1}$

Table 1. Median SFRs of full and high-SFR (sub-) samples are summarized, along with the FWHMs of both narrow and broad Gaussian components.

On the other hand, since the noise level in both stacks is comparable (given the same number of galaxies in the two bins), we can safely argue that high-SFR galaxies are (on average) characterized by larger and more prominent broad components in their [C II] spectra.

To estimate the possible effect of contamination from few single individual sources in the (sub-) samples where we found evidence of broad wings, we perform a *bootstrap* analysis. In Figs. 7.a and 7.b we show the FWHM-distributions

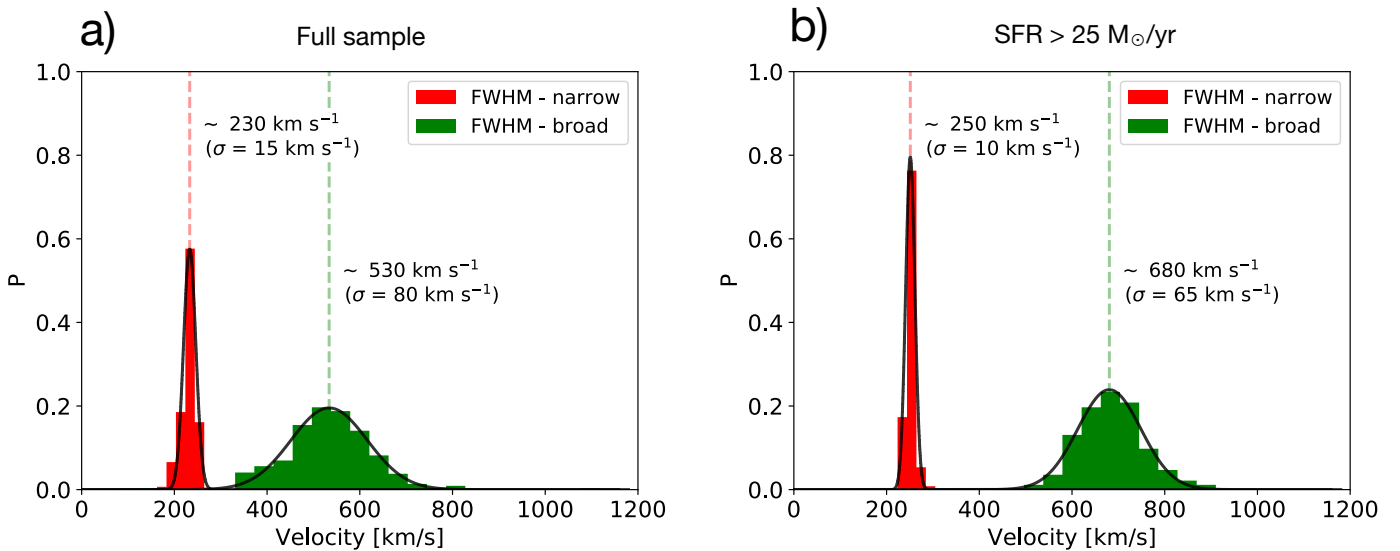


Fig. 7. FWHM-distribution of narrow (red histograms) and broad (green histograms) components obtained with jackknife analysis for the full sample (a) and the high-SFR group (b) are shown. The dashed lines represent the median values of the distribution.

of both narrow and broad components obtained with bootstrap for the full sample and the sub-sample of highly star-forming galaxies, respectively. The two panels show that for both narrow and broad components, the peaks of FWHM-distributions are well consistent with the values reported in the analysis described above (without any random replacement), indicating that no obvious dominance by a small number of galaxies is affecting our results. To improve the reliability of our measurements, we adopt the σ of the bootstrapped FWHM-distributions (see labels in Fig. 7) as uncertainties on the FWHM values of the stacked spectra reported above (see also Table 1).

We also repeat the stacking of high-SFR galaxies by combining the [C II] spectra extracted from a fixed 4×4 pixel-sized aperture (diameter of $0.6''$, i.e., slightly more than half of the averaged circularized beam) centred on the brightest pixels of the velocity-integrated [C II] maps. Apart from a small difference in terms of absolute signal, we do not find clear deviations from the stacked spectrum shown in Fig. 6.b, further suggesting that a possible contamination from faint satellites (at least on scales comparable with the beam) does not contribute significantly in building-up the observed broad component.

We note that, although the FWHM of the broad components that we measure (FWHM $< 700 \text{ km s}^{-1}$; see Table 1) is much smaller than the analogous observed in typical high- z QSOs (i.e., FWHM $\gtrsim 2000 \text{ km s}^{-1}$; see Maiolino et al. 2012; Ciccone et al. 2015; Bischetti et al. 2019), some contribution to the [C II] broadening may come from winds powered by gas accretion onto moderately massive black holes, especially in the high-SFR group. One of the objective of our survey will be indeed characterizing the AGN-activity of ALPINE galaxies, using, for instance, (i) X-ray diagnostics, and (ii) UV-spectra stacking to constrain the Type II AGN sensitive lines (e.g., HeII- $\lambda 1640 \text{ \AA}$ and CIII]- $\lambda 1908 \text{ \AA}$; see e.g., Nakajima et al. 2018; Le Fèvre et al. 2019). In addition to this, JWST will help in terms of BPT diagram classification (Baldwin et al.

1981) and observations of broad H α or [OIII]- $\lambda 5007 \text{ \AA}$ line emissions.

3.4. Stacking the cubes

As discussed in the previous sections, our stacking analysis of [C II] spectra shows that the significance of residuals from a single-Gaussian fit and broad wings on the high-velocity tails, at $v \pm \sim 500 \text{ km s}^{-1}$, increases with the SFR, indicating that star formation-driven outflows are at play in high- z normal galaxies. To better characterise the outflow properties, we explore the morphologies and spatial extensions of both the core and high-velocity wings of the [C II] line.

We therefore combine the [C II] cubes of our galaxies C_i , spectrally and spatially aligned as discussed in Sec. 3.1.1, following a vector variance-weighted stacking:

$$C_i^{\text{stack}} = \frac{\sum_{k=1}^N C_{i,k} \cdot w_{i,k}}{\sum_{k=1}^N w_{i,k}}. \quad (3)$$

Eq. 3 is a generalized version of Eq. 2 (see e.g., Fruchter & Hook 2002; Bischetti et al. 2019), where C_i^{stack} is the stacked cube composed by i slices, $C_{i,k}$ is the [C II] cube of the k -th galaxy and $w_{i,k}$ is the weighting factor defined as $w_{i,k} = 1/\sigma_{i,k}^2$. Here $\sigma_{i,k}^2$ is defined as the spatial rms estimated from a large emission-free region at each i -th slice of each k -th galaxy, and allows us to account for any frequency-dependent noise variation in the [C II] cubes.

Following the same procedure described in Sec. 3.2 and Sec. 3.3, we perform the stacking analysis of [C II] cubes for both (i) the full sample and (ii) two groups of galaxies with SFR higher/lower than the median SFR in our sample, i.e., SFR $\leq 25 \text{ M}_\odot \text{ yr}^{-1}$. We then collapse the spectral slices of the [C II] stacked cubes in the velocity ranges (i) $[-200 : +200] \text{ km s}^{-1}$, and (ii) $[-600 : -200]$, $[+200 : +600] \text{ km s}^{-1}$. Those ranges are specifically chosen to produce velocity-integrated flux maps of (i) the core of the [C II] emission, and (ii) the [C II] high-velocity tails, respectively. In Fig. 8 we show the central $8'' \times 8''$ regions of the flux maps from the stacked cubes. We find that:

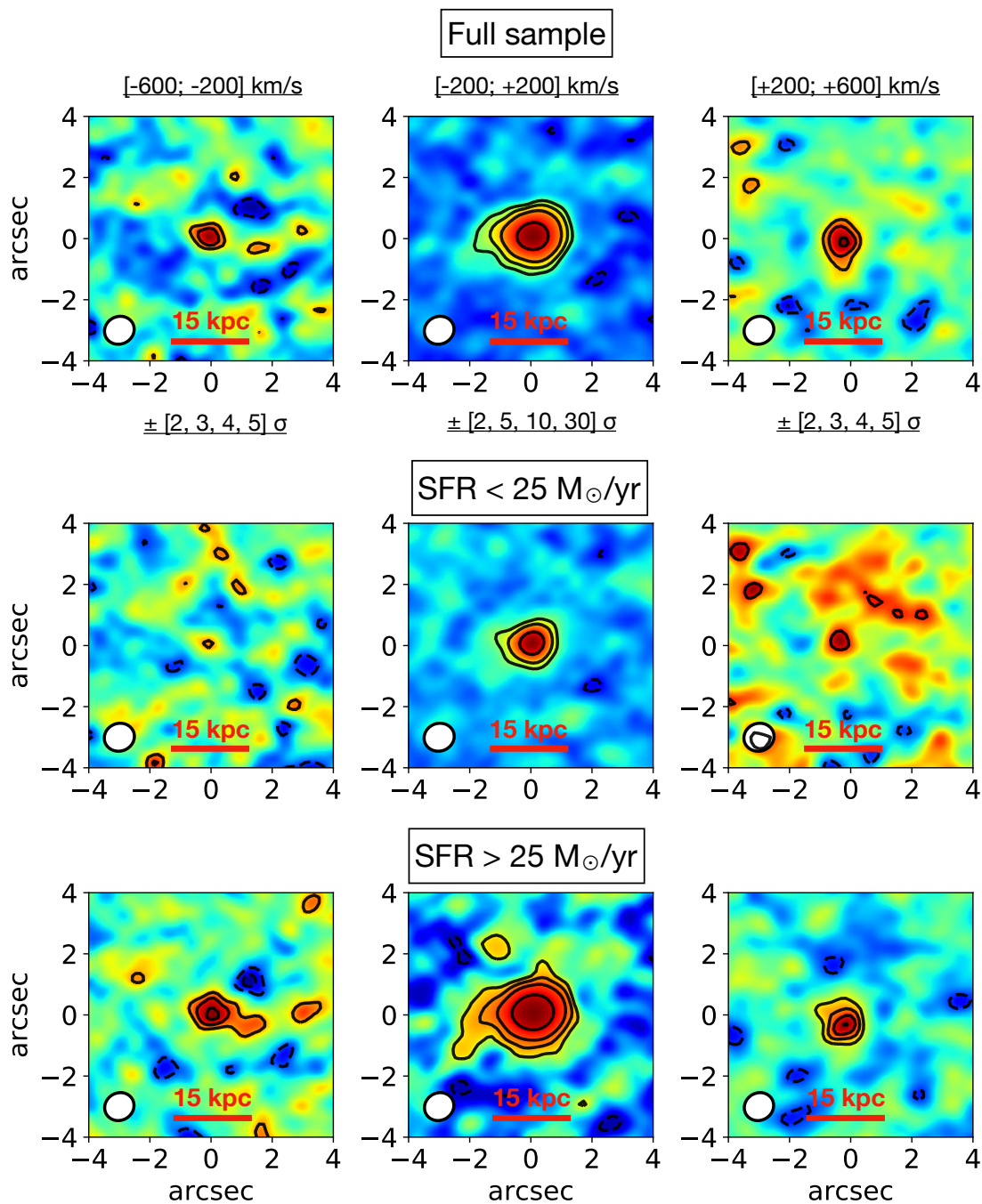


Fig. 8. Velocity-integrated [C II] flux maps (central $8'' \times 8''$ regions) are shown in different velocity ranges, from the combined cubes obtained by stacking (a) the full sample, (b) the low-SFR and (c) the high-SFR groups. Left and right panels are representative of the high-velocity tails of the [C II] emission ($[-600 : -200]$ and $[+200 : +600]$ km s $^{-1}$, respectively), while maps in the central panels trace the [C II] core ($[-200 : +200]$ km s $^{-1}$). Significance levels of the black contours are reported below the panels of a). The average synthesized beam is shown in the lower-left corners, while a reference size-scale of 15 kpc is reported at the bottom of each panel.

- [C II] emission is detected up to 4σ in the velocity-integrated maps at $[-600 : -200]$ and $[+200 : +600]$ km s $^{-1}$ of the full-sample, and up to 5σ in the high-SFR group. Only tentative detections ($\sim 2\sigma$) are revealed in the high-velocity tails of the low-SFR group (see side panels of Fig. 8). Where detected, the high-velocity [C II] emission is marginally resolved (compared with

the average beam of the observations in the stack¹¹), extending on beam-deconvolved¹² angular sizes of $\sim 0.9''$, corresponding to ~ 6 kpc at $z_{\text{med}} = 5$ (the

¹¹ The stacked synthesized beam of our observations has a major axis FWHM of $0.98''$, a minor axis FWHM of $0.89''$ and a position angle of -30 deg.

¹² We calculate beam-deconvolved sizes by fitting a 2D-Gaussian model and subtracting in quadrature the major/minor axis FWHM of our stacked synthesized beam.

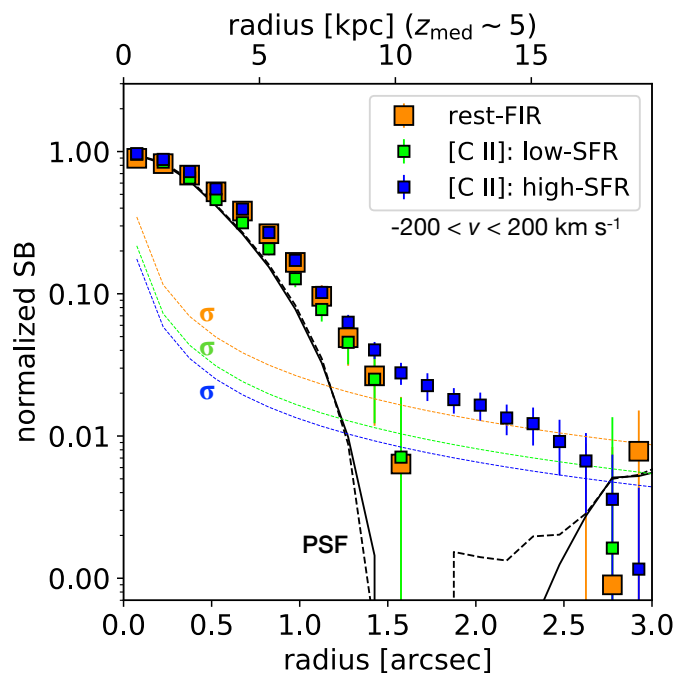


Fig. 9. Circularly averaged radial profiles computed in concentric $0.3''$ -binned annuli are shown for (i) the stacked PSF of our ALMA observations (black solid lines for galaxies in our sample, and black dashed line for ALPINE continuum-detected galaxies), (ii) the stacked FIR-continuum (orange squares) and (iii) the stacked maps of [C II] cores ($[-200 : +200]$ km s $^{-1}$) for galaxies in the low-SFR (green squares) and high-SFR (blue square) groups. Error bars are indicative of the $\pm 1\sigma$ dispersion of fluxes in each annulus, while the thin dashed lines represent the Poissonian noise associated with the radial profiles¹³.

median redshift of our galaxies);

- in the velocity-integrated image at $[-200 : +200]$ km s $^{-1}$, which traces the core of line, we detect [C II] emission at exceptionally high significance in all our three (sub-) samples, i.e., $\geq 30\sigma$ in the full sample and high-SFR bin, and $\geq 10\sigma$ in the low-SFR group (see central panels of Fig. 8). Interestingly, while in all three cases [C II] emission is fully resolved and extended on angular scales of $> 2''$ (> 15 kpc at $z_{\text{med}} = 5$), the core of [C II] line emission appears to be more extended for the high-SFR galaxies, with low-S/N (2σ) features extending up to angular scales of $\geq 3''$, corresponding to about 20 kpc at $z_{\text{med}} = 5$.

To test the reliability of these results, we repeat the analysis carrying out a *median* stacking instead of the variance-weighted mean stacking described in Eq. 3. We do not find evident deviations, confirming that our findings are not affected by outliers in the distribution.

In order to constrain with higher accuracy the typical extension of the stacked [C II] line core and quantify its dependence on the SFR (as suggested by the flux maps in Fig. 8), we compute the circularly averaged radial profiles of surface brightness (SB) from the low-velocity [C II] flux maps of our stacked (sub-) samples (see Fig. 9). We then

compare them with the radial profiles of SB extracted from the stacked point spread function (PSF)-image and the stacked FIR-continuum; the former is obtained by stacking the ALMA PSF-cubes of galaxies in our sample (using Eq. 3) and by collapsing the channels at $[-200 : +200]$ km s $^{-1}$, while the latter is obtained through a mean and rms-weighted stack of the FIR-continuum images of the 23 ALPINE continuum-detected galaxies ($\sim 90\%$ of which belongs to our high-SFR sub-sample; see details in Béthermin et al. in prep., and Khusanova et al., in prep.). Fig. 9 shows that:

- the radial profile of the stacked [C II] core in the low-SFR group is slightly more extended than the average PSF radial profile. It extends similarly to the FIR-continuum (deconvolved effective radii of $\sim 1.2''$; ~ 8 kpc at $z_{\text{med}} = 5$), suggesting that they are both tracing gas emitted on the same (galactic) scale.
- the radial profile of the stacked [C II] core in the high-SFR sub-sample extends well beyond the analogous emission from lower SFR galaxies and the stacked FIR-continuum, reaching a deconvolved effective radius of $2.3''$, corresponding to a physical distance of ~ 15 kpc at $z_{\text{med}} = 5$. While the relatively more compact profile of low-SFR galaxies could in principle be interpreted as an effect of limited sensitivity, we can safely argue that higher SFR galaxies show (on average) larger [C II] fluxes on radial scales > 10 kpc.

Our statistical detection of a low-velocity [C II] emission extended on such large physical sizes (diameter scales of ~ 30 kpc) suggests the existence of metal enriched circumgalactic halos surrounding main sequence high- z galaxies, confirming with larger statistics and significance the result obtained by Fujimoto et al. (2019), who found a 20 kpc (diameter scale) [C II] halo in the stacked cube of 18 galaxies at $5 < z < 7$ (see their discussion for an overview of the theoretical mechanisms proposed to explain the extended emission). Since outflows of processed material are needed to enrich with carbon the primordial CGM of early systems (see Fujimoto et al. 2019), the detected [C II] halo is an evidence of (i) past star formation-driven outflows, and (ii) gas mixing at play in the CGM of high- z normal star-forming galaxies (see a discussion in Sec. 4). We postpone to future papers further explorations of these findings, including, e.g., analyses of the rest-frame UV-continuum (Fujimoto et al., in prep) and Ly α stacked emissions, as well as comparisons with tailored hydrodynamical simulations (e.g., Behrens et al. 2019; Pallottini et al. 2019; Mayer et al., in prep.).

4. Discussion

The stacking analysis of [C II] spectra and cubes of ALPINE galaxies, described in Sec. 3, suggests that outflows are unequivocal in normal star-forming galaxies at $4 < z < 6$ (see possible caveats in Sec. 3.1.2). Interestingly, we find that the intensity and the significance of [C II] emission in the broad wings at the high-velocity tails of the stacked spectra/cubes increases with the SFR, supporting the star formation-induced nature of the observed outflows.

¹³ We estimate the Poissonian noise level by dividing the rms of the normalized [C II]-flux (or continuum) images by the square root of each annulus area.

Mass outflow rate and efficiency of star formation-driven outflows

To estimate the efficiency of star formation-driven outflows at play in high- z galaxies, we calculate the mass outflow rate (\dot{M}_{out}), following an approach similar to previous studies of outflows in the [C II] spectra of QSOs and normal galaxies (e.g., Maiolino et al. 2012; Cicone et al. 2015; Janssen et al. 2016; Gallerani et al. 2018; Bischetti et al. 2019).

We therefore use the luminosity of the broad [C II] component to get an estimate of the outflowing atomic gas mass, $M_{\text{out}}^{\text{atom}}$, adopting the relation from Hailey-Dunsheath et al. (2010):

$$\frac{M_{\text{out}}^{\text{atom}}}{M_{\odot}} = 0.77 \left(\frac{0.7 L_{[\text{CII}]}}{L_{\odot}} \right) \times \left(\frac{1.4 \times 10^{-4}}{X_{\text{C}^+}} \right) \times \frac{1 + 2e^{-91 K/T} + n_{\text{crit}}/n}{2e^{-91 K/T}}, \quad (4)$$

where X_{C^+} is the abundance of C^+ per hydrogen atom, n is the gas number density, n_{crit} is the critical density of the [C II] 158 μm transition (i.e., $\sim 3 \times 10^3 \text{ cm}^{-3}$), and T is the gas temperature. This relation is derived under the assumptions that:

- most of the broad [C II] emission arises from atomic gas (see a discussion in Janssen et al. 2016); specifically, 70% of the total [C II] flux (corresponding to the factor 0.7 in the first parenthesis of Eq. 4) arises from photodissociation regions (PDRs; e.g., Stacey et al. 1991, 2010), with only the remaining fraction arising from other ISM phases (see e.g., Cormier et al. 2012; Vallini et al. 2015, 2017; Lagache et al. 2018; Ferrara et al. 2019, for discussions on the relative contribution of various gas phases);
- the [C II] emission is optically thin; this sets a lower limit on $M_{\text{out}}^{\text{atom}}$ since, in case of optically thick [C II], the actual outflowing gas mass would be larger.

We use Eq. 4 assuming (i) a gas number density higher than n_{crit} (this approximation gives a lower limit on the mass of the atomic gas, as discussed in Maiolino et al. 2012), and (ii) a C^+ abundance, $X_{\text{C}^+} \sim 1.4 \times 10^{-4}$, (Savage & Sembach 1996) and a gas temperature in the range $T \sim 60 - 200 \text{ K}$, both typical of PDRs (see e.g., Kaufman et al. 1999; Hollenbach & Tielens 1999; Wolfire et al. 2003; Kaufman et al. 2006). Applying Eq. 4 to the stacked [C II] spectra of our full and high-SFR (sub-) samples (where broad components are detected) we infer a mass of the outflowing atomic gas, $M_{\text{out}}^{\text{atom}} = (2.1 \pm 0.8) \times 10^8 M_{\odot}$ for the full sample, and $M_{\text{out}}^{\text{atom}} = (2.9 \pm 1.2) \times 10^8 M_{\odot}$ for the high-SFR sub-sample. The explored range of T reflects the uncertainty reported in the estimated values of $M_{\text{out}}^{\text{atom}}$ and \dot{M}_{out} .

Then, we compute the atomic \dot{M}_{out} assuming time-averaged expelled shells or clumps (Rupke et al. 2005; Gallerani et al. 2018):

$$\dot{M}_{\text{out}} = \frac{v_{\text{out}} M_{\text{out}}}{R_{\text{out}}}, \quad (5)$$

where:

- v_{out} is the typical velocity of the atomic outflowing gas traced by [C II]. We adopt a $v_{\text{out}} \sim 500 \text{ km s}^{-1}$, based on the velocity-scale at which we observe significant peaks of deviation from a single-Gaussian model in the stacked residuals and spectra (see Fig. 2, 3.b and 5.b);

- R_{out} is the typical spatial extension of the outflow-emitting regions. We use as an estimate $R_{\text{out}} \sim 6 \text{ kpc}$, adopting the beam-deconvolved sizes derived in Sec. 3.4 from the high-velocity [C II] emission in the stacked cubes of the full and high-SFR (sub-) samples (high-velocity [C II] emission is only tentatively detected in the low-SFR bin; see Fig. 8).

We therefore estimate mass outflow rates of:

- $\dot{M}_{\text{out}} = 18 \pm 5 M_{\odot} \text{ yr}^{-1}$ for the full sample, and
- $\dot{M}_{\text{out}} = 25 \pm 8 M_{\odot} \text{ yr}^{-1}$ for the high-SFR sub-sample.

These values are lower than the median SFRs measured in the two bins, i.e., $\text{SFR}_{\text{med}} = 25 M_{\odot} \text{ yr}^{-1}$ and $\text{SFR}_{\text{med}} = 50 M_{\odot} \text{ yr}^{-1}$ in the full sample and the high-SFR group, respectively. However, we emphasise that our estimate only accounts for the atomic gas phase of the outflow, while a significant fraction of the outflowing gas is likely to be in the molecular and ionised form, as commonly observed in local star forming galaxies (e.g., Veilleux et al. 2005; Heckman & Thompson 2017; Rupke 2018). For instance, a recent work by Fluetsch et al. (2019), who study multi-phase outflows in a sample of local galaxies and AGN, shows that when including all the gas phases, the total mass loss rate increases roughly by up to 0.5 dex with respect to the value estimated from the atomic outflow only, suggesting that a coarse estimation of the total $\dot{M}_{\text{out}}^{\text{tot}}$ can be obtained multiplying by a factor of 3 the \dot{M}_{out} measured in the atomic phase.

Assuming that similar considerations apply to our sample of high- z normal galaxies, we estimate total mass outflow rates of

- $\dot{M}_{\text{out}}^{\text{tot}} \sim 55 \pm 15 M_{\odot} \text{ yr}^{-1}$ for the full sample, and
- $\dot{M}_{\text{out}}^{\text{tot}} \sim 75 \pm 24 M_{\odot} \text{ yr}^{-1}$ for the high-SFR group.

In Fig. 10 we show a comparison of our results with a compilation of local starbursts (Heckman et al. 2015) and the best-fitting relations of local AGN and normal star forming galaxies from Fluetsch et al. (2019), in the $\log(\dot{M}_{\text{out}})$ - $\log(\text{SFR})$ diagram. We find that our [C II] observations yield mass-loading factors, $\eta = \frac{\dot{M}_{\text{out}}}{\text{SFR}}$, lower than (or consistent with) the unity ($\eta^{\text{atom}} \sim 0.3 - 0.9$), in analogy with what is found in local star-forming galaxies (see e.g., García-Burillo et al. 2015; Cicone et al. 2016; Fluetsch et al. 2019; see the orange line). Assuming corrections for the multi-phase outflowing gas contribution (using the calibration discussed above; see blue dashed line in Fig. 10) we find higher mass-loading factors (see black arrows), in the range $\eta^{\text{tot}} \sim 1 - 3$, still below the η observed in local AGN ($\eta^{\text{AGN}} > 5$; see e.g., Fluetsch et al. 2019; Fiore et al. 2017 for a discussion on the dependence of η^{AGN} on the AGN properties). Therefore, even assuming that all the gas phases significantly contribute to the outflowing gas, the total mass loss rate produced by star formation-driven outflows still remains roughly comparable with the SFR. This suggests that stellar feedback is a relatively inefficient mechanism for *quenching* the star formation in normal star-forming galaxies in the early Universe and cannot be considered a dominant contributor in explaining the observed population of passive galaxies at $z \sim 2 - 3$ (e.g., Merlin et al. 2018; Santini et al. 2019; Valentino et al. 2019), but it still helps in regulating star formation as in local galaxies.

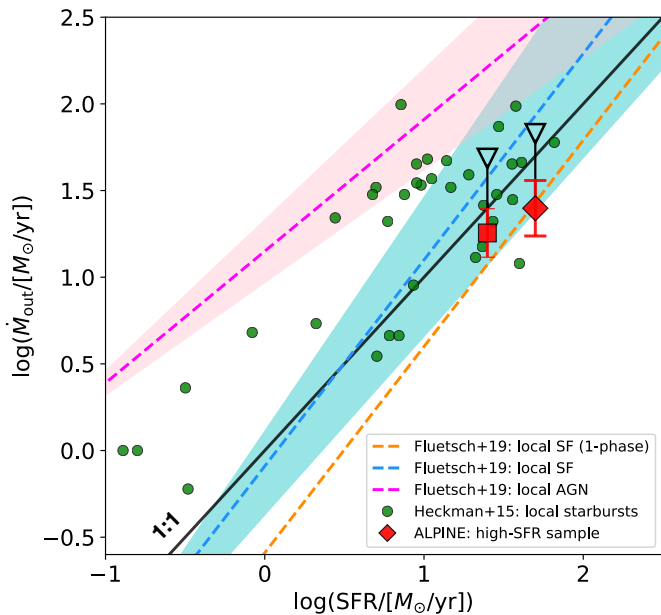


Fig. 10. A comparison of our results with a compilation of data at low- z , in the $\log(M_{\text{out}})$ - $\log(\text{SFR})$ diagram. The red square (diamond) indicates the average outflow rate for the atomic component obtained from the stacking of the full (high-SFR) sample, while red bars indicate the associated uncertainty ($\pm 1\sigma$). The black arrows show our estimate of the total \dot{M}_{out} (calculated adopting a correction for multi-phase outflows; see text). The orange (cyan) dashed line indicates the best fits for single-phase (three-phases, i.e., molecular, ionised and atomic) \dot{M}_{out} observations in local star-forming galaxies, while the magenta dashed line represents the best fit from observation of local AGN (from Fluetsch et al. 2019). Filled coloured regions are indicative of the 2σ dispersion around the best fits. The green points show the distribution of a sample of local starbursts (Heckman et al. 2015). The blue solid line indicates the 1:1 relation ($\eta = 1$).

Intergalactic/circumgalactic metal enrichment

It is still not clear whether or not the star formation-driven outflows can actually escape the DM halos and therefore effectively remove the fuel for future star formation.

On the one hand, the sensitivity of currently available data (even in the deepest integrations with ALMA, tracing both atomic and molecular FIR-lines) is far from being sufficient at revealing the spatial extension of the star formation-driven winds around individual high- z main sequence galaxies, on scales comparable with their virial radii.

On the other hand, while the stacking of ALPINE-like large samples can provide significantly improved sensitivity, the randomness of wind directions and geometries strongly challenges the detection of spatially extended outflowing gas (as seen in Sec. 3.4, where the high-velocity [C II] flux is fairly more compact than the core component).

Another way to figure out the fate of the outflows, is to compare their typical velocities, v_{out} , with the escape velocities, v_{esc} , of the DM halos. We estimate v_{esc} of the DM halos hosting the galaxies in our sample, using the formula:

$$v_{\text{esc}} = \sqrt{\frac{2 G M_{\text{DM}}}{r_{\text{DM}}}}, \quad (6)$$

where r_{DM} is the virial radius and M_{DM} is the mass of the halo. We calculate r_{DM} using the commonly adopted hypothesis of virialised halos (see e.g., Huang et al. 2017):

$$r_{\text{DM}} = \left[\frac{3 M_{\text{DM}}}{4 \pi 200 \rho_{\text{crit}}(z)} \right]^{1/3}, \quad (7)$$

where $\rho_{\text{crit}}(z)$ is the critical density of the Universe at redshift z and M_{DM} was estimated using empirically-calibrated stellar mass-halo mass (SMHM) relations (see e.g., Behroozi et al. 2013; Durkalec et al. 2015; Behroozi et al. 2019).

Galaxies in the high-SFR group of our sample, where (as discussed in Sec. 3) the signatures of atomic star formation-driven outflows are unequivocal, have stellar masses in the range $M_{\star} = 10^{10} - 10^{11.2} M_{\odot}$. Those stellar masses, according to the SMHM relation by Behroozi et al. (2019), correspond to DM halos masses in the range $M_{\text{DM}} \sim 7 \times 10^{11} - 5 \times 10^{12} M_{\odot}$ and virial radii of $r_{\text{DM}} \sim 40 - 100$ kpc (Eq. 7). Therefore, using Eq. 6, we find typical escape velocities of $v_{\text{esc}} \sim 400 - 800$ km s $^{-1}$. These values of v_{esc} , compared with the outflow velocities ($v_{\text{out}} \lesssim 500$ km s $^{-1}$) found in our stacked [C II] spectrum, suggest that a fraction of gas accelerated by star formation-driven outflows may escape the halo only in less massive galaxies (and possibly contribute to the IGM enrichment, as expected by models; e.g., Oppenheimer et al. 2010; Pallottini et al. 2014; Muratov et al. 2015), while this is unlikely to happen for the more massive galaxies. The outflowing gas that cannot escape the halo would instead be *trapped* in the CGM and eventually virialize after mixing with both the quiescent and the inflowing primordial gas, producing the large reservoir of enriched circumgalactic gas that we observe in [C II] on scales of ~ 30 kpc (see Sec. 3.4; see also a discussion in Fujimoto et al. 2019). Altogether these results confirm the expectations of cosmological simulations (see e.g., Somerville & Davé 2015; Hopkins et al. 2014; Hayward & Hopkins 2017) that the baryon cycle and the enriched gas exchanges with the CGM are at work in normal galaxies already in the early Universe.

5. Conclusions

In this work we have presented the stacking analysis of the [C II]-emission detected by ALMA in 50 main-sequence star-forming galaxies at $4 < z < 6$ (see information on the sample in Sec. 2 and Sec. 3.1.2), drawn from the ALPINE survey (Le Fèvre et al. 2019; Béthermin et al. 2019; Faisst et al. 2019). The combination of (i) a large statistics and (ii) a wealth of ancillary multi-wavelength photometry (from UV to FIR) provided by ALPINE sets the ideal conditions to progress in studying the efficiency of star formation-driven feedback and circumgalactic enrichment at early epochs. Our main findings can be summarized as follows.

- To check whether the [C II] line profiles of our galaxies can be sufficiently well described by a single-Gaussian model, we perform a variance-weighted stacking analysis of the [C II] residuals, computed by subtracting a single-component Gaussian fit to each [C II] spectrum (see Sec. 3.2). We observe typical deviations from a single-component Gaussian model, consisting of flux excesses (with peaks at $> 4\sigma$) in the high-velocity tails of the stacked residuals, at $|v| \lesssim 500$ km s $^{-1}$ (Fig. 2 and Fig. 3.b), in line with previous similar studies carried out on smaller samples (see Gallerani et al. 2018).

- We perform a variance-weighted stacking of the [C II] spectra (see Sec. 3.3) and find that the stacked [C II] profile of normal star-forming galaxies in our sample is characterized by typical signatures of outflows in its high-velocity tails. In details, we detect broad wings at velocities of few hundreds of km s^{-1} (Fig. 5), and find that the average [C II] spectrum can be accurately described by a two-component Gaussian fit (in analogy with observations of QSOs; e.g., Maiolino et al. 2012; Cicone et al. 2015; Bischetti et al. 2019), resulting in a combination of a narrow component (FWHM $\sim 230 \text{ km s}^{-1}$) and a relatively less prominent broad component (FWHM $\sim 530 \text{ km s}^{-1}$).
- We repeat the [C II] residuals/spectra stacking dividing our sample in two equally populated SFR-defined bins, using $\text{SFR}_{\text{med}} = 25 M_{\odot} \text{ yr}^{-1}$ as a threshold. We find that both (i) the significance of deviation from a single-component Gaussian model in the combined residuals (Fig. 3) and (ii) the significance of the broad wings in the high-velocity tails of the stacked [C II] spectrum (Fig. 6) increase (decrease) when stacking the sub-sample of high (low)-SFR galaxies, confirming the star formation-driven nature of these features. In particular, the stacked [C II] spectrum of high-SFR galaxies shows a broad component with a FWHM of $\sim 700 \text{ km s}^{-1}$.
- We constrain the efficiency of star formation-driven outflows at early epochs estimating the resulting mass outflow rates (see Sec. 4). We find values roughly comparable with the SFRs, yielding mass loading factor lower than (or consistent with) the unity ($\eta^{\text{atom}} \lesssim 1$), similarly to what is found in local normal star-forming galaxies (Fig. 10; see e.g., Cicone et al. 2016; Fluetsch et al. 2019). Even when considering a contribution to the outflow from multiple gas phases, the estimated mass loading factor is still below the η observed in AGN, suggesting that stellar feedback does not play a significant role in quenching galaxies at $z > 4$ and producing passive galaxies by $z \sim 2 - 3$.
- To better characterize the outflow properties and explore morphologies and spatial extensions of both the core and the high-velocity wings of the [C II] emission, we perform a stacking analysis of the datacubes (see Sec. 3.4). We find that the combined [C II] core emission ($|v| < 200 \text{ km s}^{-1}$) of galaxies in the high-SFR subsample extends on physical sizes of $\sim 30 \text{ kpc}$ (diameter scale), well beyond the the stacked FIR-continuum and the [C II] core emission of lower SFR galaxies (Fig. 9). The detection of such extended metal-enriched gas, likely tracing circumgalactic gas enriched by past outflows, corroborates previous similar studies (see Fujimoto et al. 2019), confirming that baryon cycle, metals circulation and gas mixing in the CGM are at work in normal star-forming galaxies in the early Universe.

Acknowledgements

M.G. would like to thank Andrea Ferrara, Simona Gallerani, Andrea Pallottini, Stefano Carniani, Jorryt Matthee, Emanuele Daddi and Andreas Schrubba for helpful discussions. G.C.J. and R.M. acknowledge ERC Advanced Grant 695671 “QUENCH” and support by the Science and Technology Facilities Council (STFC). M.B. acknowledges FONDECYT regular grant 1170618. E.I. acknowledges partial support from FONDECYT through grant N° 1171710. F.L., C.G., F.P. and M.T. acknowledge the support from a grant PRIN MIUR 2017. L.V. acknowledges funding from the European Union’s Horizon 2020 research and innovation program under the Marie Skłodowska-Curie Grant agreement No. 746119. S.T. acknowledges support from the ERC Consolidator Grant funding scheme (project Con-TEXT, grant No. 648179). The Cosmic Dawn Center is funded by the Danish National Research Foundation under grant No. 140. This paper is based on data obtained with the ALMA Observatory, under Large Program 2017.1.00428.L. ALMA is a partnership of ESO (representing its member states), NSF (USA) and NINS (Japan), together with NRC (Canada), MOST and ASIAA (Taiwan), and KASI (Republic of Korea), in cooperation with the Republic of Chile. The Joint ALMA Observatory is operated by ESO, AUI/NRAO and NAOJ. This program receives financial support from the French CNRS-INSU Programme National Cosmologie et Galaxies.

References

- Arnouts, S., Cristiani, S., Moscardini, L., et al. 1999, MNRAS, 310, 540
- Arribas, S., Colina, L., Bellocchi, E., Maiolino, R., & Villar-Martín, M. 2014, A&A, 568, A14
- Baldwin, J. A., Phillips, M. M., & Terlevich, R. 1981, PASP, 93, 5
- Begeman, K. G. 1989, A&A, 223, 47
- Behrens, C., Pallottini, A., Ferrara, A., Gallerani, S., & Vallini, L. 2019, MNRAS, 486, 2197
- Behroozi, P., Wechsler, R. H., Hearin, A. P., & Conroy, C. 2019, MNRAS, 1134
- Behroozi, P. S., Wechsler, R. H., & Conroy, C. 2013, ApJ, 770, 57
- Benson, A. J., Bower, R. G., Frenk, C. S., et al. 2003, ApJ, 599, 38
- Bigiel, F., Leroy, A. K., Walter, F., et al. 2011, ApJ, 730, L13
- Bischetti, M., Maiolino, R., Carniani, S., et al. 2019, A&A, 630, A59
- Bower, R. G., Benson, A. J., Malbon, R., et al. 2006, MNRAS, 370, 645
- Bradač, M., Garcia-Appadoo, D., Huang, K.-H., et al. 2017, ApJ, 836, L2
- Brinchmann, J., Charlot, S., White, S. D. M., et al. 2004, MNRAS, 351, 1151
- Bruzual, G. & Charlot, S. 2003, MNRAS, 344, 1000
- Capak, P. L., Carilli, C., Jones, G., et al. 2015, Nature, 522, 455
- Carniani, S., Maiolino, R., Amorin, R., et al. 2018, MNRAS, 478, 1170
- Carniani, S., Marconi, A., Biggs, A., et al. 2013, A&A, 559, A29
- Cattaneo, A., Faber, S. M., Binney, J., et al. 2009, Nature, 460, 213
- Chabrier, G. 2003, PASP, 115, 763
- Chisholm, J., Tremonti, C. A., Leitherer, C., & Chen, Y. 2017, MNRAS, 469, 4831
- Chisholm, J., Tremonti, C. A., Leitherer, C., et al. 2015, ApJ, 811, 149
- Chisholm, J., Tremonti, C. A., Leitherer, C., & Chen, Y. 2016, MNRAS, 463, 541
- Cicone, C., Maiolino, R., Gallerani, S., et al. 2015, A&A, 574, A14
- Cicone, C., Maiolino, R., & Marconi, A. 2016, A&A, 588, A41
- Cormier, D., Leboutteiller, V., Madden, S. C., et al. 2012, A&A, 548, A20
- Daddi, E., Bournaud, F., Walter, F., et al. 2010, ApJ, 713, 686
- de Blok, W. J. G., Walter, F., Smith, J. D. T., et al. 2016, AJ, 152, 51
- De Breuck, C., Williams, R. J., Swinbank, M., et al. 2014, A&A, 565, A59

- Decarli, R., Walter, F., Venemans, B. P., et al. 2018, *ApJ*, 854, 97
- Dekel, A. & Silk, J. 1986, *ApJ*, 303, 39
- Di Teodoro, E. M. & Fraternali, F. 2015, *MNRAS*, 451, 3021
- Durkalec, A., Le Fèvre, O., de la Torre, S., et al. 2015, *A&A*, 576, L7
- Erb, D. K. 2015, *Nature*, 523, 169
- Fabian, A. C. 2012, *ARA&A*, 50, 455
- Faisst, A., Bethermin, M., Capak, P., et al. 2019, arXiv e-prints, arXiv:1901.01268
- Ferrara, A., Vallini, L., Pallottini, A., et al. 2019, *MNRAS*, 1964
- Feruglio, C., Fiore, F., Carniani, S., et al. 2018, *A&A*, 619, A39
- Fiore, F., Feruglio, C., Shankar, F., et al. 2017, *A&A*, 601, A143
- Fluetsch, A., Maiolino, R., Carniani, S., et al. 2019, *MNRAS*, 483, 4586
- Fruchter, A. S. & Hook, R. N. 2002, *PASP*, 114, 144
- Fujimoto, S., Ouchi, M., Ferrara, A., et al. 2019, arXiv e-prints, arXiv:1902.06760
- Gallerani, S., Pallottini, A., Feruglio, C., et al. 2018, *MNRAS*, 473, 1909
- García-Burillo, S., Combes, F., Usero, A., et al. 2015, *A&A*, 580, A35
- Hailey-Dunsheath, S., Nikola, T., Stacey, G. J., et al. 2010, *ApJ*, 714, L162
- Hashimoto, T., Laporte, N., Mawatari, K., et al. 2018, *Nature*, 557, 392
- Hasinger, G., Capak, P., Salvato, M., et al. 2018, *ApJ*, 858, 77
- Hayward, C. C. & Hopkins, P. F. 2017, *MNRAS*, 465, 1682
- Heckman, T. M., Alexandroff, R. M., Borthakur, S., Overzier, R., & Leitherer, C. 2015, *ApJ*, 809, 147
- Heckman, T. M., Armus, L., & Miley, G. K. 1990, *ApJS*, 74, 833
- Heckman, T. M. & Thompson, T. A. 2017, arXiv e-prints, arXiv:1701.09062
- Hollenbach, D. J. & Tielens, A. G. G. M. 1999, *Reviews of Modern Physics*, 71, 173
- Hopkins, P. F., Kereš, D., Oñorbe, J., et al. 2014, *MNRAS*, 445, 581
- Hopkins, P. F., Quataert, E., & Murray, N. 2012, *MNRAS*, 421, 3522
- Hopkins, P. F., Torrey, P., Faucher-Giguère, C.-A., Quataert, E., & Murray, N. 2016, *MNRAS*, 458, 816
- Huang, K.-H., Fall, S. M., Ferguson, H. C., et al. 2017, *ApJ*, 838, 6
- Ilbert, O., Arnouts, S., McCracken, H. J., et al. 2006, *A&A*, 457, 841
- Inoue, A. K., Tamura, Y., Matsuo, H., et al. 2016, *Science*, 352, 1559
- Janssen, A. W., Christopher, N., Sturm, E., et al. 2016, *ApJ*, 822, 43
- Jones, G. C., Carilli, C. L., Shao, Y., et al. 2017, *ApJ*, 850, 180
- Kaufman, M. J., Wolfire, M. G., & Hollenbach, D. J. 2006, *ApJ*, 644, 283
- Kaufman, M. J., Wolfire, M. G., Hollenbach, D. J., & Luhman, M. L. 1999, *ApJ*, 527, 795
- Kennicutt, Robert C., J. 1998, *ARA&A*, 36, 189
- Kohandel, M., Pallottini, A., Ferrara, A., et al. 2019, *MNRAS*, 487, 3007
- Krumholz, M. R. & McKee, C. F. 2005, *ApJ*, 630, 250
- Lagache, G., Cousin, M., & Chatzikos, M. 2018, *A&A*, 609, A130
- Le Fèvre, O., Lemaux, B. C., Nakajima, K., et al. 2019, *A&A*, 625, A51
- Le Fèvre, O., Tasca, L. A. M., Cassata, P., et al. 2015, *A&A*, 576, A79
- Leroy, A. K., Walter, F., Brinks, E., et al. 2008, *AJ*, 136, 2782
- Leroy, A. K., Walter, F., Sandstrom, K., et al. 2013, *AJ*, 146, 19
- Mac Low, M.-M. & Ferrara, A. 1999, *ApJ*, 513, 142
- Maiolino, R., Carniani, S., Fontana, A., et al. 2015, *MNRAS*, 452, 54
- Maiolino, R., Gallerani, S., Neri, R., et al. 2012, *MNRAS*, 425, L66
- Matthee, J., Sobral, D., Boogaard, L. A., et al. 2019, *ApJ*, 881, 124
- McMullin, J. P., Waters, B., Schiebel, D., Young, W., & Golap, K. 2007, in *Astronomical Society of the Pacific Conference Series*, Vol. 376, *Astronomical Data Analysis Software and Systems XVI*, ed. R. A. Shaw, F. Hill, & D. J. Bell, 127
- Merlin, E., Fontana, A., Castellano, M., et al. 2018, *MNRAS*, 473, 2098
- Muratov, A. L., Kereš, D., Faucher-Giguère, C.-A., et al. 2015, *MNRAS*, 454, 2691
- Nakajima, K., Schaerer, D., Le Fèvre, O., et al. 2018, *A&A*, 612, A94
- Noeske, K. G., Weiner, B. J., Faber, S. M., et al. 2007, *ApJ*, 660, L43
- Oppenheimer, B. D. & Davé, R. 2006, *MNRAS*, 373, 1265
- Oppenheimer, B. D., Davé, R., Kereš, D., et al. 2010, *MNRAS*, 406, 2325
- Pallottini, A., Ferrara, A., Decataldo, D., et al. 2019, *MNRAS*, 487, 1689
- Pallottini, A., Gallerani, S., & Ferrara, A. 2014, *MNRAS*, 444, L105
- Riechers, D. A., Carilli, C. L., Capak, P. L., et al. 2014, *ApJ*, 796, 84
- Rodighiero, G., Daddi, E., Baronchelli, I., et al. 2011, *ApJ*, 739, L40
- Rubin, K. H. R., Prochaska, J. X., Koo, D. C., et al. 2014, *ApJ*, 794, 156
- Rubin, K. H. R., Weiner, B. J., Koo, D. C., et al. 2010, *ApJ*, 719, 1503
- Rupke, D. 2018, *Galaxies*, 6, 138
- Rupke, D. S., Veilleux, S., & Sanders, D. B. 2005, *ApJS*, 160, 115
- Santini, P., Merlin, E., Fontana, A., et al. 2019, *MNRAS*, 486, 560
- Savage, B. D. & Sembach, K. R. 1996, *ARA&A*, 34, 279
- Shapley, A. E., Steidel, C. C., Pettini, M., & Adelberger, K. L. 2003, *ApJ*, 588, 65
- Silk, J. & Mamon, G. A. 2012, *Research in Astronomy and Astrophysics*, 12, 917
- Smit, R., Bouwens, R. J., Carniani, S., et al. 2018, *Nature*, 553, 178
- Somerville, R. S. & Davé, R. 2015, *ARA&A*, 53, 51
- Speagle, J. S., Steinhardt, C. L., Capak, P. L., & Silverman, J. D. 2014, *ApJS*, 214, 15
- Stacey, G. J., Geis, N., Genzel, R., et al. 1991, *ApJ*, 373, 423
- Stacey, G. J., Hailey-Dunsheath, S., Ferkinhoff, C., et al. 2010, *ApJ*, 724, 957
- Stanley, F., Jolly, J. B., König, S., & Knudsen, K. K. 2019, arXiv e-prints, arXiv:1908.11395
- Steidel, C. C., Erb, D. K., Shapley, A. E., et al. 2010, *ApJ*, 717, 289
- Steidel, C. C., Shapley, A. E., Pettini, M., et al. 2004, *ApJ*, 604, 534
- Sugahara, Y., Ouchi, M., Harikane, Y., et al. 2019, arXiv e-prints, arXiv:1904.03106
- Sugahara, Y., Ouchi, M., Lin, L., et al. 2017, *ApJ*, 850, 51
- Talia, M., Brusa, M., Cimatti, A., et al. 2017, *MNRAS*, 471, 4527
- Talia, M., Mignoli, M., Cimatti, A., et al. 2012, *A&A*, 539, A61
- Talia, M., Pozzi, F., Vallini, L., et al. 2018, *MNRAS*, 476, 3956
- Tasca, L. A. M., Le Fèvre, O., Ribeiro, B., et al. 2017, *A&A*, 600, A110
- Valentino, F., Tanaka, M., Davidzon, I., et al. 2019, arXiv e-prints, arXiv:1909.10540
- Vallini, L., Ferrara, A., Pallottini, A., & Gallerani, S. 2017, *MNRAS*, 467, 1300
- Vallini, L., Gallerani, S., Ferrara, A., Pallottini, A., & Yue, B. 2015, *ApJ*, 813, 36
- Veilleux, S., Cecil, G., & Bland-Hawthorn, J. 2005, *ARA&A*, 43, 769
- Wagg, J., Wiklind, T., Carilli, C. L., et al. 2012, *ApJ*, 752, L30
- Wolfire, M. G., McKee, C. F., Hollenbach, D., & Tielens, A. G. G. M. 2003, *ApJ*, 587, 278
- Woosley, S. E., Heger, A., & Weaver, T. A. 2002, *Reviews of Modern Physics*, 74, 1015

-
- ¹ Observatoire de Genève, Université de Genève, 51 Ch. des Maillettes, 1290 Versoix, Switzerland
e-mail: michele.ginolfi@unige.ch
 - ² Cavendish Laboratory, University of Cambridge, 19 J. J. Thomson Ave., Cambridge CB3 0HE, UK
 - ³ Kavli Institute for Cosmology, University of Cambridge, Madingley Road, Cambridge CB3 0HA, UK
 - ⁴ Aix Marseille Univ, CNRS, CNES, LAM, Marseille, France
 - ⁵ Osservatorio di Astrofisica e Scienza dello Spazio - Istituto Nazionale di Astrofisica, via Gobetti 93/3, I-40129, Bologna, Italy
 - ⁶ University of Bologna, Department of Physics and Astronomy (DIFA), Via Gobetti 93/2, I-40129, Bologna, Italy
 - ⁷ Institute for Cosmic Ray Research, The University of Tokyo, Kashiwa-no-ha, Kashiwa 277-8582, Japan
 - ⁸ Department of Astronomy, School of Science, The University of Tokyo, 7-3-1 Hongo, Bunkyo, Tokyo 113-0033, Japan
 - ⁹ IPAC, California Institute of Technology, 1200 East California Boulevard, Pasadena, CA 91125, USA
 - ¹⁰ University of Padova, Department of Physics and Astronomy Vicolo Osservatorio 3, 35122, Padova, Italy
 - ¹¹ Kavli Institute for the Physics and Mathematics of the Universe, The University of Tokyo, Kashiwa, Japan 277-8583 (Kavli IPMU, WPI)
 - ¹² Caltech Optical Observatories, Cahill Center for Astronomy and Astrophysics 1200 East California Boulevard, Pasadena, CA 91125, USA
 - ¹³ Centro de Astronomia (CITEVA), Universidad de Antofagasta, Avenida Angamos 601, Antofagasta, Chile
 - ¹⁴ Instituto de Física y Astronomía, Universidad de Valparaíso, Gran Bretaña 1111, Playa Ancha, Valparaíso, Chile
 - ¹⁵ Department of Physics and Astronomy, University of Massachusetts, Amherst, MA 01003, USA
 - ¹⁶ Department of Physics, University of California, Davis, One Shields Ave., Davis, CA 95616, USA
 - ¹⁷ Department of Astronomy, University of Florida, 211 Bryant Space Sciences Center, Gainesville, FL 32611 USA
 - ¹⁸ Cosmic Dawn Center (DAWN)
 - ¹⁹ Niels Bohr Institute, University of Copenhagen, Lyngbyvej 2, DK-2100 Copenhagen, Denmark
 - ²⁰ Leiden Observatory, Leiden University, PO Box 9500, 2300 RA Leiden, The Netherlands